Indian J Phys
https://doi.org/10.1007/s12648-025-03885-6

ORIGINAL PAPER

Probing the physical properties of the chalcogenide-based double perovskites Ba_2NbBiS_6 and Ba_2TaSbS_6: DFT investigation

Z Bouguerra[1]*, I Bouzateur[2], H Bennacer[1,3], A Boukortt[1], M A Ouali[3], M Hadjab[3] and M I Ziane[4]

[1]Elaboration and Physical, Mechanical, and Metallurgical Characterization of Material Laboratory, University of Mostaganem, ECP3M, 27000 Mostaganem, Algeria

[2]Modelling and Simulation of Magnetic Properties of Heterostructures Laboratory, Faculty of Sciences and Technology, Tissemsilt University, Bougara, Algeria

[3]Department of Electronics, Faculty of Technology, University of M'sila, University Pole, Road Bordj-Bou-Arreridj, 28000 M'sila, Algeria

[4]Laboratory of Electrical and Materials Engineering, LGEM, Higher School of Electrical and Energetic Engineering of Oran, Oran, Algeria

Received: 29 June 2025 / Accepted: 19 November 2025

Abstract: Using density functional theory (DFT) with the GGA-PBESol, LDA, and TB-mBJ approximations, this paper thoroughly examines the structural, elastic, optoelectronic, and thermoelectric properties of chalcogenide-double perovskites Ba_2NbBiS_6 and Ba_2TaSbS_6, with the view to their potential use in optoelectronic and photovoltaic devices. Based on the calculation results, both compounds achieve the Born stability criteria and negative formation energy values, confirming their thermodynamic stability. Additionally, the elastic criteria analysis shows that the materials exhibit strong resistance to volume deformation while remaining ductile and demonstrate anisotropic characteristics, as seen through the ELATools software. Furthermore, the electronic band structure and density of states were investigated. The Ba_2NbBiS_6 compound exhibits an indirect band gap (L–X) of 1.58 eV (mBJ-GGA) and 1.45 eV (mBJ-LDA), while the Ba_2TaSbS_6 compound shows an indirect band gap (L–Γ) of 1.45 eV (mBJ-GGA) and 1.28 eV (mBJ-LDA). Analysis of the (DOS) and the electronic band structure revealed the contribution of 4d_Nd for Ba_2NbBiS_6 and 5d_Ta for Ba_2TaSbS_6. Furthermore, optical parameters derived from the dielectric function, including reflectivity, absorption coefficient, and refractive index were predicted. As a result, both compounds exhibit strong photon absorption extending from the visible to ultraviolet regions, with absorption coefficients of 342.03 $\times$ 10^4/cm for Ba_2NbBiS_6 and 333.92 $\times$ 10^4/cm for Ba_2TaSbS_6, indicating their high potential for optoelectronic devices. In addition, thermoelectric properties such as the Seebeck coefficient, electrical conductivity, thermal conductivity, ZT merit, and power factor were evaluated. The results provide valuable insights that may guide future experimental studies on these promising materials.

Keywords: DFT; Chalcogenide; Double Perovskite; Solar cells

1. Introduction

The demand for clean, sustainable, and renewable energy, also known as green energy, has increased due to climate change and the environmental pollution caused by global energy sources. Global warming is one of the most pressing challenges we face and it can be addressed by increasing the use of green energy sources, creating cutting-edge energy storage technologies, and improving energy-saving techniques [1–5]. Modern energy solutions rely on solar energy because of its abundant supply, cleanliness, and absence of pollution-related drawbacks.

Perovskite solar cells (PSCs) have attracted a lot of interest from the scientific community in recent years due to their inexpensive cost, straightforward production process, and remarkable photoelectric conversion efficiency (PCE) [6, 7]. The PCE of PSCs has recently marked a significant achievement, surpassing 25.2% [8]. This fact highlights that perovskites among the most efficient materials used in solar cell industry. The major obstacle to the performance of PSCs is the large number of internal and interfacial defects arising from uncontrolled

*Corresponding author, E-mail: zakarya.bouguerra.etu@univ-mosta.dz

Published online: 03 December 2025

crystallization of perovskite, Li et al. [9] highlighted a new technique that uses five-fluoropyridinic acid (FPA) to enhance perovskite crystal growth and minimize the defects, achieving an energy conversion efficiency of 25.37% and maintaining 93% stability over 3000 h. The demand for sustainable and green energy solutions has led to unprecedented attempts to use materials for clean energy technologies, such as hydrogen storage, worldwide. Perovskite hydrides, specifically alkali metal XNH_6 (where X = Li, Na, K), demonstrate promising hydrogen capacities [10]. In recent study conducted by Mursaleen et al. [11] a family of fluoroperovskites $A_2FeB'F_6$ (A = K, Na: B′ = Ag, Au) with remarkable magnetic and electrical properties, make them attractive options for the development of advance spintronic devices.

The exceptional charge transporting capabilities and adjustable bandgaps across the full visible spectrum are among the remarkable characteristics of all-inorganic perovskite [12], highlighting their promising potential in a wide range of electronic devices, including light sensors [13], solar cells [14], and X-ray scintillators [15]. Silicon solar cells retained first place in manufacturing because of their low cost and high performance for many years [6, 16, 17], until new studies appeared on other perovskites [16–20]. Different structural phases, including cubic, tetragonal, and orthorhombic ones, are feasible in perovskites' cubic lattice-nested octahedral layers [18–20]. One of the problems faced by perovskite materials is the presence of lead, which reduces the stability of the compounds over time. Long-term stability problems and decreased device performance may arise from this instability [21, 22]. In contrast to single perovskite oxides, double perovskite oxides have a broad range of physical characteristics and a more extensive and customizable range of ion combinations [23, 24].

The DFT has been a significant tool in the evaluation of double perovskite with the A_2BXY_6 composition [22, 25–28]. It provides valuable insight into charge transport mechanisms and interfacial electronics properties, providing a robust theoretical basis for improving the performance of applications such as triboelectric nanogenerators [29]. Researchers have found this type of calculation promising are now using it to study hydrogen storage materials, such as K_2ZnH_4 and Rb_2ZnH_4, which have shown promising results, high stability, and semiconductor properties [30]. Perovskite semiconductors, specifically, ABX_3 and A_2BXY_6, are highly promising for advancing the performance of photovoltaic and optoelectronic devices [31–33]. Although there is a range of perovskite materials, halide double perovskite has gained importance due to their structural stability, wide tunability, and potential for optoelectronic and thermoelectric applications. Recent DFT studies have indicated that X_2ScTlI_6 (X = Rb, Cs) possesses a stable structure with promising electronic and optical properties with band gaps of 2.79 eV and 2.81 eV, respectively [34].

The viability of using a particular class of ABX_3 perovskites as absorbers in solar cells was studied theoretically by Sun et al. [35] (A stands for Ca, Sr, and Ba; B represents Ti, Zr, and Hf; and X stands for S and Se). They developed a number of compounds, including $BaZrS_3$, which was marketed as a very promising candidate. After that, it was produced in lab tests, and the findings, which were reported in [36, 37]. Exhibited a direct bandgap ranging from 1.73 to 1.85 eV. In their study, Ju et al. [38] investigated 18 different ABX_3 chalcogenide perovskites, however, they proposed that by combining $SrSnS_3$ and $SrSnSe_3$ in specific ratios, the band gap could be tuned to achieve optimal sunlight absorption. Similarly, Bouguerra et al. [39] suggested chalcogenide-based perovskite with an indirect band gap of 3.02 eV for $CaSiS_3$ and 1.71 eV for $CaSiSe_3$. In research and applications, materials with wider band gaps are often overlooked, but with the correct amount of pressure, they can be effectively modified to match vital specifications [40]. Despite this, no chalcogenide perovskite based solar cells have been reported to date [41]. Moreover, both $BaZrS_3$ and $SrSn(S,Se)_3$ lack single-pair s-orbitals, which is crucial for achieving high efficiency in organic–inorganic hybrid perovskites (OIHP). The study also explores chemically modifying the B-site cations in $BaZrS_3$, specifically replacing Zr (IV) with M(III) and M(V), where M(III) = Sb^{3+} or Bi^{3+} and M(V) = Nb^{5+} or Ta^{5+}. Furthermore, thermoelectric simulations on chalcogen-doped SrI_2 systems with S and Se have demonstrated enhanced electrical conductivity and increased power factor within the 200–800 K range [42].

Thus, A_2BXY_6 can be extended to many compounds through the multiple occupancy of B/X sites and A/Y sites [43, 44], in these complex materials, double perovskites based on chalcogenides are undeniably effective. Their properties have demonstrated their potential as efficient absorbers, and their use in solar cells has yielded promising results. Sun et al. [45], stated that these chalcogenide double perovskites possess exceptional optoelectronic properties, including, balanced electron and hole effective masses, direct band gaps, and high optical absorption, all with thermodynamic stability.

One of the most important compounds that demonstrated both flexibility and high absorption, as reported by Agiorgousis et al. [46]. Furthermore, the issue of lead toxicity remains a significant challenge for the International Lead Health Partnership (ILHP). Three double perovskite compounds $Cs_2AgBiBr_6$ [47, 48], $Cs_2AgBiCl_6$ [47, 49], and $Cs_2AgSbCl_6$ [47, 50], have been successfully synthesized. Notably, these compounds possess indirect bandgaps due to the mismatch between Ag orbitals and Sb/

Bi s-orbitals at the band edges, limiting their effectiveness as absorbers in thin-film solar cells. However, when Sb/Bi is replaced with In in Cs_2AgInX_6 (X = Cl, Br), direct bandgaps are observed, making these compounds more suitable for solar cell applications [47, 51]. According to recent simulation studies, Ba_2MgXO_6 (with X = S or Se) is considered a semiconductor, showing a direct band gap value of 0.33–0.66 eV and an absorption coefficient of 10^5 cm^{-3} [52].

Recently, Baaziz et al. [41] conducted a DFT study on the structural, electronic, and optical properties of both Ba_2NbBiS_6 and Ba_2TaSbS_6 where they found indirect band gap (L–X) of 1.680 eV and 1.529 eV, respectively, with high absorption coefficients in the Ultraviolet spectrum. The elastic and thermoelectric properties of these materials have not been investigated, which is necessary to determine their applicability in solar cells. Thus, this research provides an in-depth analysis on the physical characteristics of both compounds, including their elastic and thermoelectrical features. This study was carried out using a first-principles method. Our theoretical study reduced range values for both GGA and LDA compared to earlier research while the use of TB-mBJ demonstrated improved computational accuracy. Perovskites can adopt various structural configurations, with the most common being cubic and orthorhombic. The ideal cubic structure, Fm $\overline{3}$ m, was selected for double perovskites Ba_2NbBiS_6 and Ba_2TaSbS_6 because it is the high-symmetry parent phase in this material family and offers high stability. This choice simplifies computational modeling, provides a solid basis for exploring their intrinsic electronic and charge transfer properties, and allows for a direct comparison with similar double perovskites reported in the literature.

2. Computational details

The physical properties, such as the structural, electronic, optical, and thermoelectric properties of the double perovskites Ba_2NbBiS_6 and Ba_2TaSbS_6, were evaluated using first-principles calculations implemented in the WIEN2K code [53] using the FP-LAPW method [54] within the framework of density functional theory (DFT) [55, 56]. To determine the structural parameters, the generalized gradient approximation of Perdew-Becke-Ernzerhof (GGA-PBESol) [57] and the Local Density Approximation (LDA) [58] were employed to describe the exchange–correlation potential. The GGA and LDA formulations of the exchange–correlation potential are expressed as follows [59, 60]:

$$V_{\mu\nu}^{XC(GGA)} = \int dr\, \phi_\mu(r)\, v_{XC}^{GGA}(r)\, \phi_\nu(r) \tag{1}$$

$$V_{xc}^{LDA}(r) = -\frac{4}{3} c_X \rho(r)^{1/3} + V_C^{LDA}(r) \tag{2}$$

The Tran–Blaha-modified Becke–Johnson (TB-mBJ) [61] was used to predict the electronic structure and optical properties. The electronic transport characteristics of these double chalcogenide perovskites were computed using the BoltzTraP2 code [62]. The TB-mBJ potential is written as:

$$V_{x,\sigma}^{mBj}(r) = cv_{x,\sigma}^{BR}(r) + (3c-2)\frac{1}{\pi}\sqrt{\frac{5}{12}\sqrt{\frac{2\tau_\sigma(r)}{\rho_\sigma(r)}}} \tag{3}$$

where ρ_σ is the electron density, τ_σ is the kinetic-energy, and $v_{x,\sigma}^{BR}$ is the Becke-Roussel potential [63], and c (c = 1) is a system-dependent quantity that represents the original value of the Becke-Johnson potential.

In our calculation, $K_{max} = 7/R_{MT}$ was selected (where the average radius of the spherical muffin tin is known as R_{MT}, which depends on the chosen atoms of the compound, and the vector wave K has a maximum value called K_{max}). The Fourier expansion of the charge density was limited to $G_{max} = 12$ a.u.$^{-1}$. Up to $l_{max} = 10$, the valence wave functions in the muffin-tin spheres were expanded. The Muffin-tin radii were set in the range of [1.8–2.51 a.u] for the elements (Ba, Nb, Bi, Ta, Sb, and S), according to their atomic numbers. We used 10 × 10 × 10 k-points meshes in the irreducible wedge of the Brillouin zone, and 10 × 10 × 10 × 10 k-points in the Irreducible Brillouin Zone (IBZ) to analyze the optical and thermoelectric properties.

3. Results and discussion

3.1. Structure and geometrical estimation

To determine the ground state structural parameters, such as the lattice constant (*a*), bulk modulus (*B*), and the derivative compressibility (*B'*), the energy-volume curve for both compounds Ba_2NbBiS_6 and Ba_2TaSbS_6 was calculated using the generalized gradient approximation of the Perdew-Becke-Ernzerhof (GGA-PBESol) and the local density approximation (LDA) [64]. Figure 1(a, b) illustrates the relaxed crystal configurations using VESTA, and the optimized volume curves that correspond with each one are displayed in Fig. 1(c), in the cubic structure that belongs to the Fm $\overline{3}$ m space group (No. 225). These parameters were obtained by fitting with the Murnaghan equation of state [65] given by Eq. 4, which entails

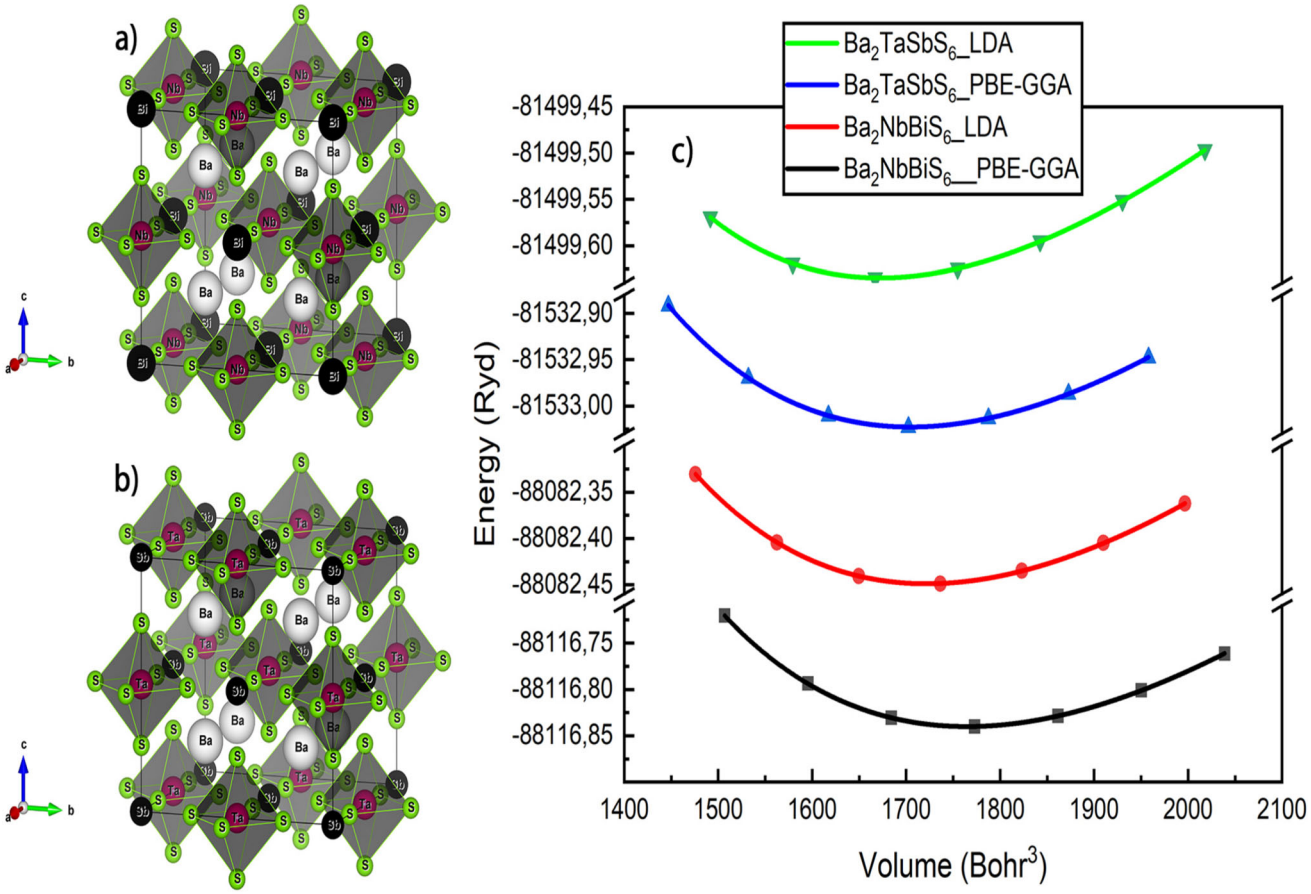

Fig. 1 Detailed crystal structures of (**a**) Ba_2NbBiS_6 and (**b**) Ba_2TaSbS_6, along with (**c**) optimized configurations

minimizing the total energy associated with the unit cell's volume. It's apparent that the calculations for GGA-PBE-Sol indicated that the stability is much higher than it is for LDA, as lower values indicate higher stability. The calculated structural parameters of these two relaxed structures in comparison with other theoretical data are listed in Table 1.

$$E(V) - E(V_0) = \frac{B_0 V}{B_0'}\left[\frac{(V_0/V)^{B_0'}}{B_0'} + 1\right] - \frac{B_0 V_0}{B_0' - 1} \tag{4}$$

Using the GGA-PBESol, the ground state energy of Ba_2NbBiS_6 is found to be − 88,116.84 Ry, with a lattice constant of 10.15 Å. This compound exhibits a bulk modulus of 69.87 GPa and a compressibility *B'* of 4.31. Similarly, Ba_2TaSbS_6 has a ground state energy

Table 1 Optimized structural parameters of Ba_2NbBiS_6 and Ba_2TaSbS_6

		Lattice constant a = b = c (Å)	*B* (GPa)	*B'*	E_0 (Ry)	ΔH_f (eV)
Ba_2NbBiS_6	GGA-PBESol	10.15	69.87	4.31	− 88,116.84	− 21.19
		10.1584 [41]	71.0646 [41]	4.4521 [41]		
	LDA	10.07	74.10	4.33	− 88,082.45	
		10.0762 [41]	76.2068 [41]	4.4782 [41]		
Ba_2TaSbS_6	GGA-PBESol	10.03	74.10	4.21	− 81,533.02	− 18.70
		10.0292 [41]	74.8654 [41]	4.3735 [41]		
	LDA	9.97	79.23	4.55	− 81,499.63	
		9.9641 [41]	79.5824 [41]	4.3908 [41]		

of − 81,533.02 Ry, a lattice constant of 10.03 Å, and a bulk modulus value of 74.10 GPa with compressibility *B'* of 4.21. In comparison, the LDA yielded ground state energy of − 88,082.45 Ry at 10.07 Å and − 81,499.63 Ry at 9.97 Å for Ba_2NbBiS_6 and Ba_2TaSbS_6, respectively. To further evaluate the structural stability of these compounds, the tolerance factor (t) and octahedral factor (μ) were calculated using Eqs. (5) and (6) [66]. The ionic radius of the A, B, and X ions is designated as r_A, r_B, and r_X.

$$t = \frac{r_A + r_X}{\sqrt{2}(r_B + r_X)} \tag{5}$$

$$\mu = \frac{r_B}{r_X} \tag{6}$$

For perovskites to form and remain stable in a cubic structure, the ideal tolerance factor typically falls within the range 0.825 and 1.059, while the acceptable interval for the octahedral factor is from 0.415 to 0.895 [67, 68]. The tolerance and octahedral factors are shown in Table 1, demonstrating their stability within the cubic configuration. The obtained results indicate that Ba_2NbBiS_6 exhibits a higher structural stability with a tolerance factor of approximately 0.97, whereas Ba_2TaSbS_6 shows a slightly lower value of around 0.87.

To assess the stability nature of the structure being examined, the formation energies of the two compounds are calculated. A negative ΔH_f typically indicates that the compound may be synthetically accessible from its constituent elements, while the positive formation energy value suggests thermodynamic instability and a tendency for decomposition [69]. Moreover, the positive values indicate less or no stability because of the absence of harmony between the atoms of the compounds being studied, which can cause melting, fracturing, or decomposition of materials. A higher negative formation energy in materials usually correlates with a greater elastic modulus, suggesting that strong atomic bonds are essential for both thermodynamic and mechanical stability [70]. The formation energy ΔH_f for Ba_2NbBiS_6 and Ba_2TaSbS_6 is given with the following relation [64].

$$\Delta H_f = E_T - (2E_{Ba} + E_{Nb/Ti} + E_{Bi/Sb} + 6E_S) \tag{7}$$

where E_T is the total energy of the crystal. The energies of discrete atoms are indicated by E_{Ba}, E_{Nb}, E_{Ti}, E_{Bi}, E_{Sb}, and E_S. Formation energy negative values indicate the complete dynamic stability of Ba_2NbBiS_6 and Ba_2TaSbS_6 materials.

3.2. Elastic attributes

The elastic constants can be used to determine the mechanical characteristics of a solid-state material and evaluate how it responds to external forces [4] using the Wien2k package, which is utilized to assess the elastic constants of Ba_2NbBiS_6 and Ba_2TaSbS_6. These cubic structures mechanical stability is defined by the elastic constants C_{11}, C_{12}, and C_{44} [71], which are summarized in Table 2 using GGA-PBESol. They use their elastic constants to verify the Born-Hung stability criterion in the situation of stable cubic crystals, as follows: [72].

$$C_{11} > 0, \quad C_{44} > 0, \quad (C_{11} - C_{12}) > 0, \quad (C_{11} + 2C_{12}) > 0 \tag{8}$$

According to Table 2, the studied compounds are mechanically stable because they satisfy all stability criteria listed in Eq. (8). The Hill Shear (G_H) and Hill Bulk moduli (B_H), in addition to the Hill Young's modulus (E_H) for Ba_2TaSbS_6, are higher than those of Ba_2NbBiS_6 (as shown in Table 2). These parameters can be computed as follows [73]:

$$B_H = \frac{C_{11} + 2C_{12}}{3} \tag{9}$$

$$G_H = \frac{G_V + G_R}{2} \tag{10}$$

$$E_H = \frac{9B_G}{3B + G} \tag{11}$$

A material's bulk modulus can be used to assess its resistance to volume deformation. A higher bulk modulus value increases the fracture resistance strength. Furthermore, the Shear modulus parameter indicates the extent of plastic deformation in a material. A lower Shear modulus value suggests that the material can be easily bent [74]. On the other hand, the Youngs modulus (E) parameter characterizes the material's flexibility. The smaller the E value, the more flexible the material is [75]. The values are summarized in Table 2. The Ba_2TaSbS_6 has the larger values of B_H, G_H, and E_H of 74.90, 37.18, and 95.70 GPa, respectively, more than Ba_2NbBiS_6, which has a value of 70.39, 31.50, and 82.22 GPa, correspondingly. The values

Table 2 Mechanical parameters of Ba_2NbBiS_6 and Ba_2TaSbS_6 using the GGA-PBESol

Materials	Ba_2NbBiS_6	Ba_2TaSbS_6
C_{11} (GPa)	139.13	151.77
C_{12} (GPa)	36.02	36.46
C_{44} (GPa)	22.39	27.51
Bulk Modulus (B) (GPa)	70.39	74.90
Shear Modulus (G) (GPa)	31.50	37.18
Young Modulus (E) (GPa)	82.22	95.70
Poisson's coefficient (ν)	0.31	0.29
B/G	2.23	2.01
Debye temperature (T_D) (K)	284.74 ± 300	306.71 ± 300

of ductility ratio (B_H/G_H, which is also called the Pugh ratio), Poisson's ratio (ν), and the Cauchy pressure (C_{12}–C_{44}) > 0 disclose the ductile and the brittle nature of the two studied materials [76]. Both compounds achieved values of ν > 0.26 and B/G > 1.75. In Figs. 2 and 3, we can visually see how shear modulus, Poisson's ratio, Pugh's ratio, and Young's modulus are displayed in the *XY*, *XZ*, and *YZ* planes using the ElATools.

Young's modulus (E_H) is used to quantify the stiffness of the compound, with Crystal anisotropy revealed by the degree to which the three-dimensional Young's moduli diverge from a perfect sphere [77, 78]. The calculated Young's modulus according to (100), (010), and (001)

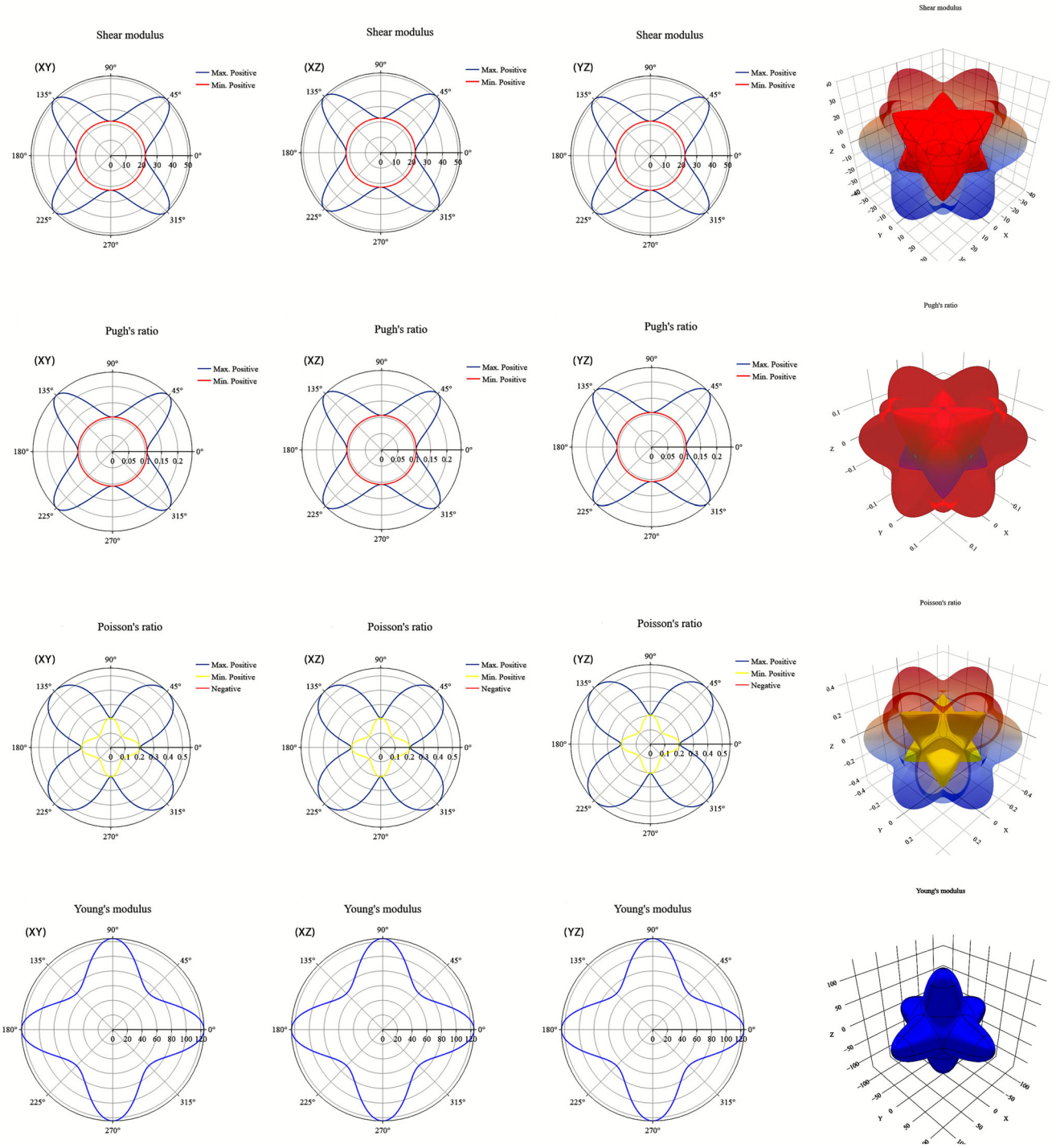

Fig. 2 The shear constant, Pugh ratio, Poisson's ration and young's modulus of Ba_2NbBiS_6 are represented in 2D and 3D

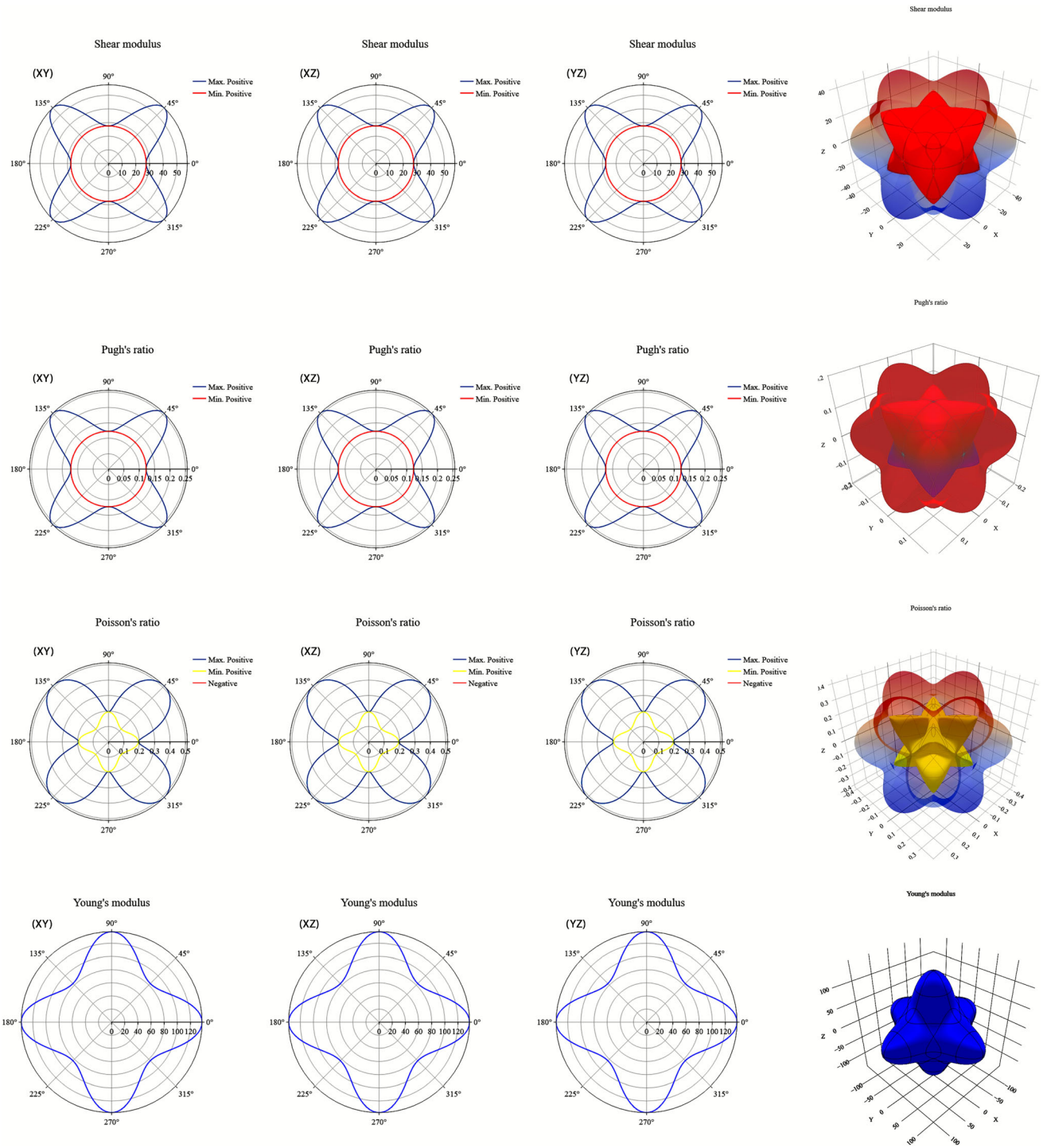

Fig. 3 The shear constant, Pugh ratio, Poisson's ration and young's modulus of Ba_2TaSbS_6 are represented in 2D and 3D

plane shows non-spherical contrast surfaces, indicating anisotropy using the ELATE module [79], as evidenced by Figs. 2 and 3. In addition, a large degree of anisotropy may be seen between these two double perovskites and a close simulation as a result of the similarity of bonding properties in the adjacent (*XY*), (*XZ*), and (*YZ*) atomic planes to each compound. This noticeable anisotropy indicates that these compounds' mechanical response varies with direction, which is a vital factor for their practical applications. The stability of materials under stress is impacted by significant anisotropy, which causes them to deform or cleave along particular crystallographic orientations more readily. Recognizing this behavior is crucial for designing devices such as optoelectronic or thermoelectric components,

where consistent mechanical performance and durability are essential. The high values calculated for Young's modulus, 95.70 GPa for Ba_2TaSbS_6 and 82.22 GPa for Ba_2NbBiS_6 (Table 2), indicate the stiffness of the materials. It is possible to determine the type of crystal bond in a material by using the Poisson coefficient value, which has covalent (0.1), ionic (0.25), or metallic (0.33) bonds [39, 80, 81]. Ba_2NbBiS_6 and Ba_2TaSbS_6 exhibit ionic bonding, as demonstrated by their Poisson coefficient. The temperature of a crystal's maximum normal mode of vibration is known as the Debye temperature (T_D), and it establishes a correlation between the elastic characteristics and thermodynamic parameters, including phonons, and thermal conductivity [39, 82, 83]. Once the type of bond in the compounds has been identified using the Poisson ratio, evaluating its strength can be done by examining the values associated with the Debye temperature (T_D) [39]. Based on our calculations, Ba_2TaSbS_6 exhibits stronger ionic bonding compared to Ba_2NbBiS_6 (T_D = 284.74 K), with the highest thermal decomposition temperature (T_D) of 306.71 K.

4. Electronic properties

Understanding the material electronic properties in detail is pivotal as it provides information on the band structure and the total density of states TDOS, which describes the allowed energy levels for electrons [84–88]. A thorough understanding is essential for evaluating the potential of an electronic band structure for use in optoelectronic devices [89]. It's clear that the bandgap of both double perovskites exhibits semiconductor behavior as illustrated in Fig. 4(a, b) within the mBJ-GGA and summarized in Table 3. The Ba_2NbBiS_6 compound shows an indirect bandgap of approximately 1.58 eV, with the valence band maximum (VBM) located at the high-symmetry point X, while the conduction band minimum (CBM) is positioned at the maximum symmetry L point. Ba_2TaSbS_6 also displays an indirect bandgap of about 1.45 eV, with the VBM located at the L point and CBM at the Γ point. On the other hand, the mBJ-LDA gives the same behavior as mBJ-GGA for each compound, with a difference in the gap values for Ba_2NbBiS_6 and Ba_2TaSbS_6 of 1.45 and 1.28 eV, respectively, as we can see in Table 3. The only primary difference between the compounds is the substitution of NbBi with TaSb elements, which is a key factor responsible for this difference in the band gap in the same cubic structure. The main cause of this is the difference in the electronic distributions of the constituent elements ([Nb]: $4d^4\ 5s^1$; [Bi]: $4f^{14}\ 5d^{10}\ 6s^2\ 6p^3$; [Ta]: $4f^{14}\ 5d^3\ 6s^2$; [Sb]: $4d^{10}\ 5s^2\ 5p^3$). Using the same approach, Baaziz et al. [41] found that both compounds displayed indirect bandgaps (Table 3). Electrons in indirect bandgap semiconductors require an additional momentum shift to transition from the valence to conduction bands [90], whereas this shift is not required in a direct bandgap semiconductor.

In Fig. 5(a, b), we depicted both of total and partial density of states (TDOS and PDOS) versus the energy for Ba_2NbBiS_6 and Ba_2TaSbS_6 compounds. While the conduction band represents the energy levels where electrons can move freely, the electrons in the valence band contribute to the overall stability of the structure [90].

From the TDOS, we observe that both double perovskites are semiconductors. Furthermore, both valence and conduction bands are primarily composed of 4d_Nd states, with the contribution of 5p_Bi states, with a minor contribution from 3p_S states in the valence band (VB), and 4d_Ba states in the conduction bands (CB) for Ba_2NbBiS_6. The VBM mainly arises from the antibonding interaction between the 4d orbital of Nd and the 3p orbital of the S atom, which is consistent with previous findings. Conversely, the TDOS for Ba_2TaSbS_6 reveals that both valence and conduction bands are primally composed of 5d_Ta states, with the contribution of 3p_S states and a minor intervention from 5p_Sb on the VB side, and 4d_Ba states in the CB. The obtained result highlights that the VBM is formed by the involvement of the 5d_Ta lone pair and the 3p_S orbital. However, Baaziz et al. [41] attribute the VBM state to the participation of the 5s orbital of the Sb atom, which contrasts with our findings and may explain the difference in band gap for Ba_2TaSbS_6.

This behavior differs from that observed in $CH_3NH_3PbI_3$, where the VBM originates from the I–p orbital and the antibonding state of Pb's s lone pair [41, 91]. Meanwhile, in both Ba_2NbBiS_6 and Ba_2TaSbS_6, the CBM is predominantly influenced by the 4d_Ba states.

5. Optoelectronic properties

The goal of this research is to investigate the optical properties of Ba_2NbBiS_6 and Ba_2TaSbS_6 in order to evaluate their potential optoelectronic devices. Several parameters are calculated, starting with the complex dielectric constant $\varepsilon(\omega) = \varepsilon_1(\omega) + i\varepsilon_2(\omega)$, followed by the absorption coefficient $\alpha(\omega)$, the reflection $R(\omega)$, and the quantified refractive index $n(\omega)$, which collectively make the vast study easier [92–95]. All the optical parameters shown in Fig. 6 were investigated at an energy range from 0 to 16 eV, except for the absorption coefficient, which was analyzed from 0 to 20 eV. The extracted static values of $\varepsilon_1(0)$, $n(0)$, and $R(0)$ are summarized in Table 4.

The complex dielectric function $\varepsilon(\omega)$, which describes how a material interacts with light and makes it possible to calculate other optical parameters, can be used to

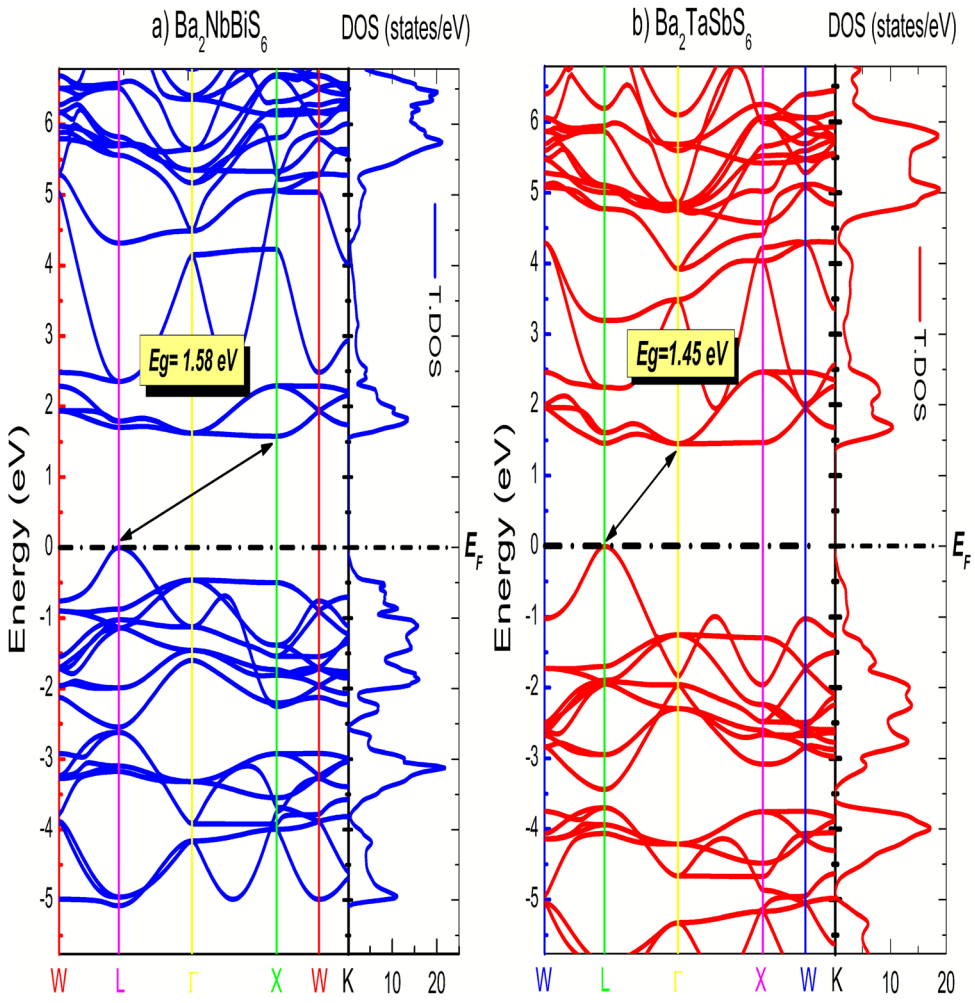

Fig. 4 Band structures using the mBJ-GGA for (**a**) Ba_2NbBiS_6 and (**b**) Ba_2TaSbS_6 compounds

Table 3 The calculated band gaps in eV of Ba_2NbBiS_6 and Ba_2TaSbS_6 double perovskites (Indirect gap denoted as '*i*' and '*d*' for direct gap)

Materials	Eg (eV)				
	GGA-PBESol	mBJ-GGA	LDA	mBJ-LDA	Experimental Works
Ba_2NbBiS_6	0.62_i *(L–X)*	1.58_i *(L–X)*	0.57_i *(L–X)*	1.45_i *(L–X)*	–
Other work	0.628_i *(L–X)* [41]	1.680_i *(L–X)* [41]	0.578_i *(L–X)* [41]	1.566_i *(L–X)* [41]	–
Ba_2TaSbS_6	0.60_i *(L–Γ)*	1.45_i *(L–Γ)*	0.48_i *(L–Γ)*	1.28_i *(L–Γ)*	–
Other work	0.683_i *(L–X)* [41]	1.529_i *(L–X)* [41]	0.668_i *(L–X)* [41]	1.527_i *(L–X)* [41]	–
Ba_2GaNbS_6	–	1.2613_d [113]	–	–	–
Ca_2GaNbS_6	–	1.3728_d [113]	–	–	–
$CH_3NH_3PbI_3$	–	–	–	–	1.63 eV [114]

determine the optical characteristics of materials [96]. Additionally, it was used to comprehend how materials interact with electromagnetic waves. Where $\varepsilon_1(\omega)$ and $\varepsilon_2(\omega)$ denote the real and imaginary parts, in sequence, of the dielectric functions. Using the Kramers–Kronig relations, the $\varepsilon_1(\omega)$ can be calculated from the imaginary part $\varepsilon_2(\omega)$. The real part $\varepsilon_1(\omega)$ represents how the medium polarizes in response to an electric field [78, 97]. The imaginary part $\varepsilon_2(\omega)$ illustrates the transition from the occupied states to vacant states as light traverses the medium [78, 98, 99], which can be obtained by the following equations [100, 101]:

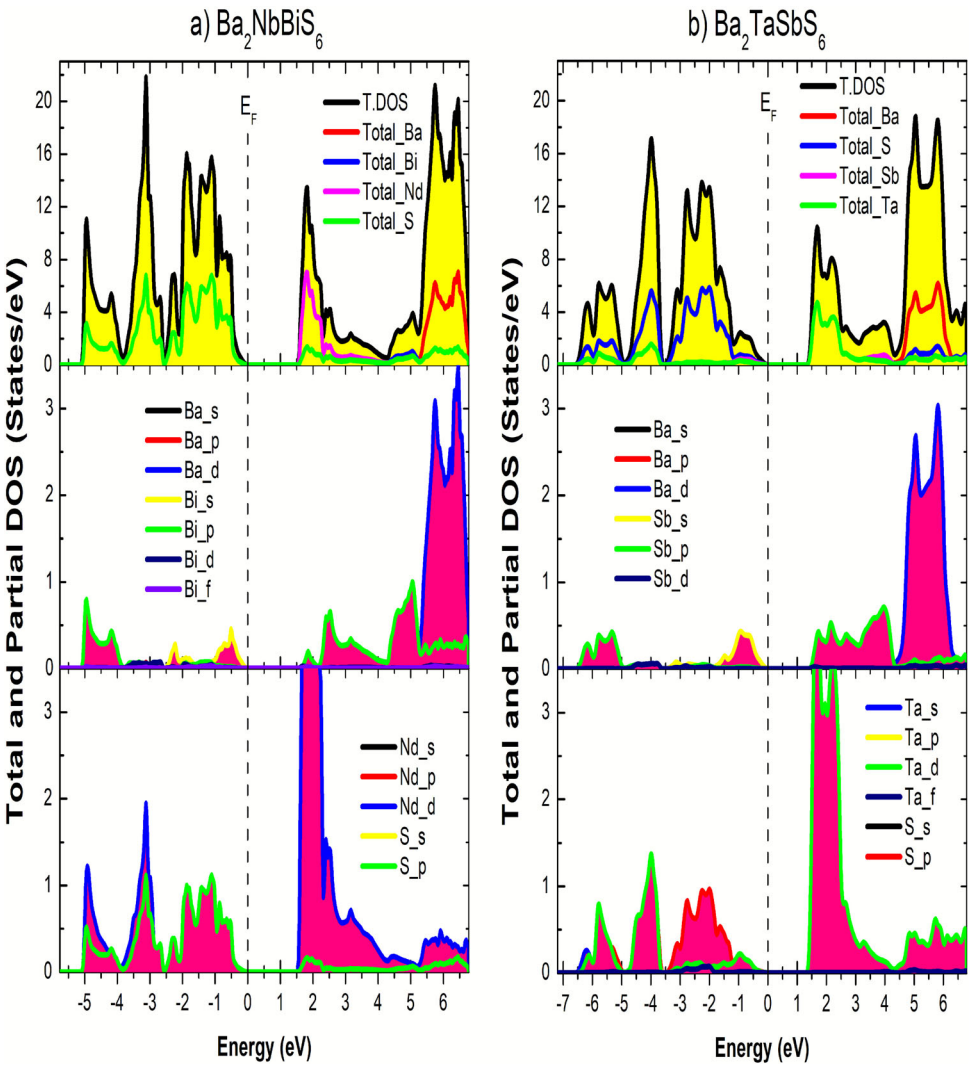

Fig. 5 TDOS and PDOS calculated using the mBJ-GGA approach for double perovskite of (**a**) Ba_2NbBiS_6 and (**b**) Ba_2TaSbS_6

$$\varepsilon_1(\omega) = 1 + \frac{2}{\pi} P \int_0^{\infty} \frac{\omega \prime \varepsilon_2(\omega')}{\omega' 2 - \omega^2} d\omega' \tag{12}$$

$$\varepsilon_2(\omega) = \frac{Ve^2}{2\pi\hbar m^2\omega^2} \int d^3k \sum_{nn'} \left|\langle kn|p|kn\rangle'\right|^2 f(kn) \times (1 - f(kn'))\delta(E_{kn} - E_{kn'} - \hbar\omega) \tag{13}$$

The values of $\varepsilon_1(\omega)$ and $\varepsilon_2(\omega)$ are illustrated in Fig. 6(a, b), with positive value of $\varepsilon_1(\omega)$ from 0 to 3.22 eV for Ba_2NbBiS_6 and 3.85 eV for Ba_2TaSbS_6, which indicates the semiconducting nature of these two double perovskites. At zero frequency, the values of $\varepsilon_1(0)$ for both Ba_2NbBiS_6 and Ba_2TaSbS_6 are 7.69 and 7.96, respectively. The obtained real part shows a high value at 2.54 eV for Ba_2NbBiS_6 and 2.27 eV for Ba_2TaSbS_6. From the $\varepsilon_1(\omega)$, the $\varepsilon_2(\omega)$ is obtained by solving the Kramer-Kronig relation [102]. Furthermore, the initial absorption peak is the first peak of the $\varepsilon_2(\omega)$ [71]. The Ba_2NbBiS_6 first absorption peak is found at 2.22 eV, whereas the Ba_2TaSbS_6 first absorption peak is found at 2.35 eV.

The amount of light that a material can absorb at a given frequency is determined by the absorption coefficient $\alpha(\omega)$ [32]. The light absorption process varies among materials, depending on the energy band gap values. These values signify the absorption thresholds of the materials. The interaction between photons and electrons enables materials to absorb light, but only if this interaction surpasses the threshold value. Using Eq. (14) [82], the absorption coefficient can be calculated.

$$\alpha(\omega) = \sqrt{2}\left[\sqrt{\varepsilon_1^2(\omega) + \varepsilon_2^2(\omega)} - \varepsilon_1(\omega)\right]^{1/2} \tag{14}$$

The representation of the absorption coefficient is demonstrated in Fig. 6(c). Ba_2TaSbS_6 has the first high absorption coefficient $\sim 96.18 \times 10^4$/cm in the range of [1.48–5.89 eV], and Ba_2NbBiS_6 has an absorption

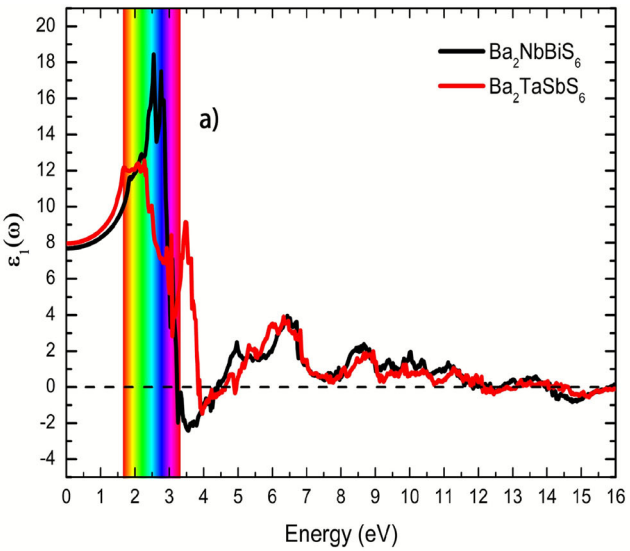
a)
Ba_2NbBiS_6
Ba_2TaSbS_6
$\varepsilon_1(\omega)$
Energy (eV)

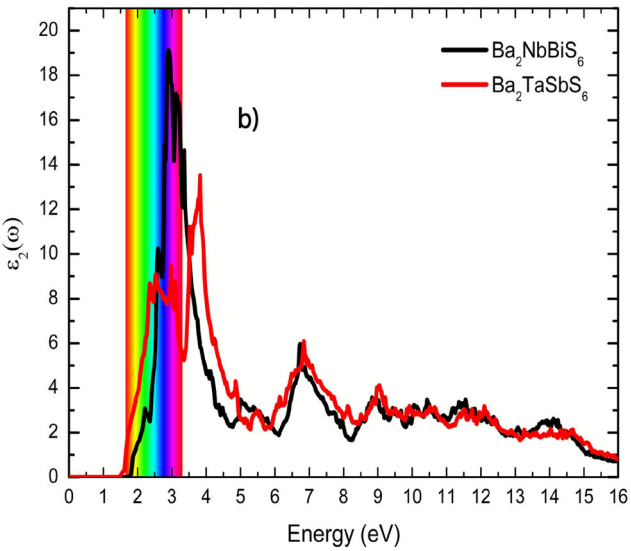
b)
Ba_2NbBiS_6
Ba_2TaSbS_6
$\varepsilon_2(\omega)$
Energy (eV)

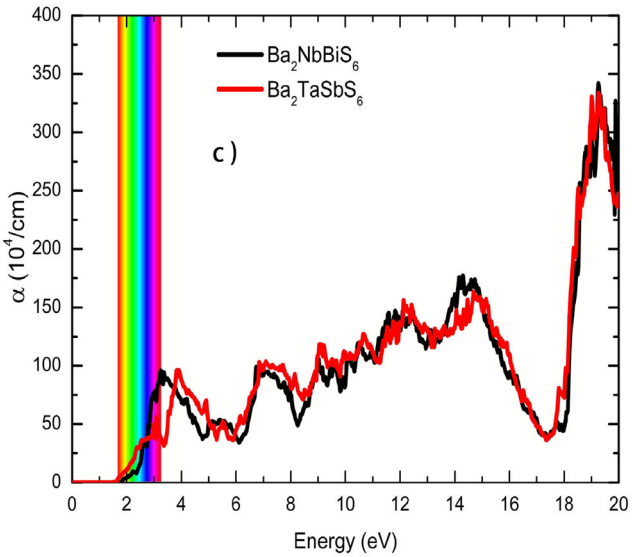
c)
Ba_2NbBiS_6
Ba_2TaSbS_6
α (10^4/cm)
Energy (eV)

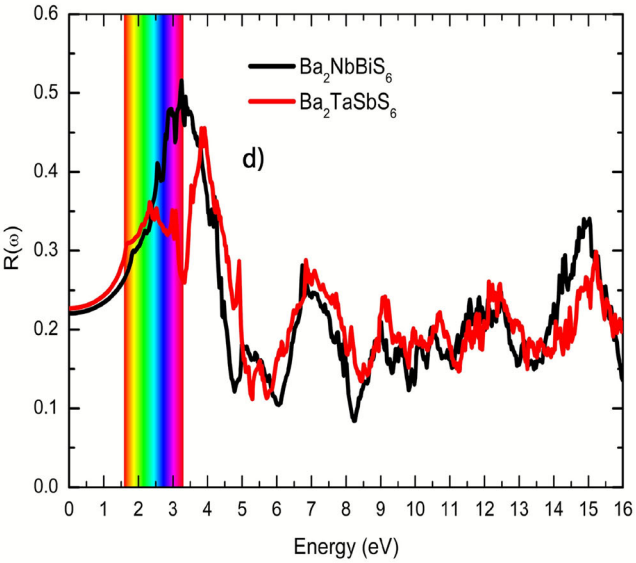
d)
Ba_2NbBiS_6
Ba_2TaSbS_6
R(ω)
Energy (eV)

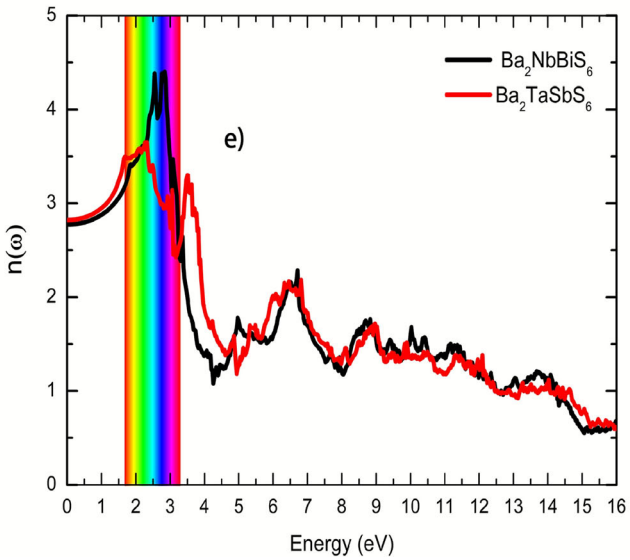
e)
Ba_2NbBiS_6
Ba_2TaSbS_6
n(ω)
Energy (eV)

◀**Fig. 6** (**a**) Real and (**b**) imaginary parts of the dielectric function, (**c**) absorption coefficient, (**d**) reflectivity, and (**e**) refractive index for Ba_2NbBiS_6 and Ba_2TaSbS_6

Table 4 Computed $\varepsilon_1(\omega)$, $n(\omega)$, and $R(\omega)$ at zero frequency using the (mBJ-GGA) approximations for the compounds Ba_2NbBiS_6 and Ba_2TaSbS_6

Materials	$\varepsilon_1(0)$	n(0)	R(0)
Ba_2NbBiS_6	7.69	2.77	0.22 (22%)
Other work	7.413 [41]	3.756 [41]	
Ba_2TaSbS_6	7.96	2.82	0.22 (22%)
Other work	7.187 [41]	3.793 [41]	
Ca_2GaNbS_6	6.936 [113]	2.634 [113]	20.22% [113]
Sr_2GaNbS_6	6.959 [113]	2.638 [113]	20.28% [113]
Ba_2GaNbS_6	7.223 [113]	2.687 [113]	20.94% [113]

coefficient ~ 95.81 × 10^4/cm in the range of [1.73–5.89 eV]. These energy intervals include the visible and ultraviolet spectra, which suggests that these two compounds are promising candidates for solar cell applications. The high absorption is observed at 19.25 eV with a value of 342.03 × 10^4/cm for Ba_2NbBiS_6 and 333.92 × 10^4/cm for Ba_2TaSbS_6. Although these high-energy transitions lie beyond the visible solar spectrum, their high $\alpha(\omega)$ values in the visible and near-UV range (see Fig. 6(c)) imply that even thin layers of these materials can absorb incident photons efficiently. This property is particularly advantageous in thin films and tandem solar cells with wide-bandgap top layers, where the top cell, acting as a high-bandgap material, collects the high-energy photons of the solar spectrum and transmits lower-energy photons to an adjacent cell with a smaller bandgap. Compared to their findings, our absorption coefficient exceeds the values that reported by Baaziz et al. [41], who obtained values of 301.4 × 10^4/cm and 294.3 × 10^4/cm (mBJ–GGA), successively.

Figure 6(d) shows both compounds' reflectivity $R(\omega)$. Notably, Ba_2NbBiS_6 and Ba_2TaSbS_6 have computed reflectivity of 0.22 and 0.23 at null frequency R(0), consecutively. It is evident that in the observed energy area, which includes the visible or ultraviolet regions, the $R(\omega)$ of the two materials that depend on photon energy rises with extremely small values. The high values of reflectivity are approximately 0.52 for Ba_2NbBiS_6 and about 0.46 for Ba_2TaSbS_6.

From the refractive index $n(\omega)$ in Fig. 6(e), the calculated static refractive index n(0) is sequentially 2.77 and 2.82 for Ba_2NbBiS_6 and Ba_2TaSbS_6, and it continues to increase in the visible and ultraviolet regions until reaching their maximum values of 4.4 and 3.65, respectively. We notice a similar shape by comparing the result of refractive indices in Fig. 6(e) with the real part plot in Fig. 6(a). The following formula can be used to find the reflectivity $R(\omega)$ and the refractive index $n(\omega)$ [103].

$$R(\omega) = \left[\frac{\sqrt{\varepsilon_1(\omega) + i\varepsilon_2(\omega)} - 1}{\sqrt{\varepsilon_1(\omega) + i\varepsilon_2(\omega)} + 1} - \varepsilon_1(\omega)\right]^2 \quad (15)$$

$$n(\omega) = \left[\frac{\varepsilon_1(\omega)}{2} + \frac{\sqrt{\varepsilon_1^2(\omega) + \varepsilon_2^2(\omega)}}{2}\right]^{1/2} \quad (16)$$

6. Thermoelectric properties

We have expanded our investigation to include the thermoelectric characteristics of the proposed materials. Our study involves the Seebeck coefficient (S), electrical conductivity (σ/τ), and thermal conductivity (κ/τ) at temperatures of 300, 500, and 700K. Except of thermal conductivity, all of these properties must be higher in a thermoelectric material [104].

Figure 7(a, b) displays the Seebeck coefficient (S) versus the chemical potential at various temperature values. The Seebeck coefficient can signify the type of charge carrier, with n-type for a negative sign and p-type for a positive sign, and for high-quality thermoelectric materials, this coefficient value should be in the range of 200 μV/K [105, 106]. The value of S switches from the p-type region to the n-type region, and there is a significant saw tooth deviation. The value of S changes between ± 1.57 mV/K for Ba_2NbBiS_6 and between ± 1.41 mV/K for Ba_2TaSbS_6 at 300K, which indicates that the majority of charge carriers shift from electrons to holes. The concentration gradient decreases as temperatures rise to 500K and 700K, which attempts to equalize the distribution of charge carriers. As seen in the figure, the Seebeck coefficient for both materials didn't exhibit the same trend in the thermoelectric voltage response to a temperature difference, they displayed anisotropic behavior. Additionally, this variation could be due to a difference in the band structure characteristics and the material's electrical conductivity. As shown in Fig. 8(a), the Seebeck coefficient (S) is plotted as function of temperature ranging 300–900 K, where it rises in an approximately linear way this. This upward trend highlights the growing influence of carrier diffusion at evaluated temperatures, which enhanced thermoelectric efficiency, starting at 63.97 μV/K for Ba_2NbBiS_6 and 41.91 μV/K for Ba_2TaSbS_6 at 300 K, and reaching 104.14 and 100.76 μV/K at 900 K, respectively.

The calculated electrical conductivity (σ/τ) in Fig. 7(c, d) showed that these two compounds have a high electrical

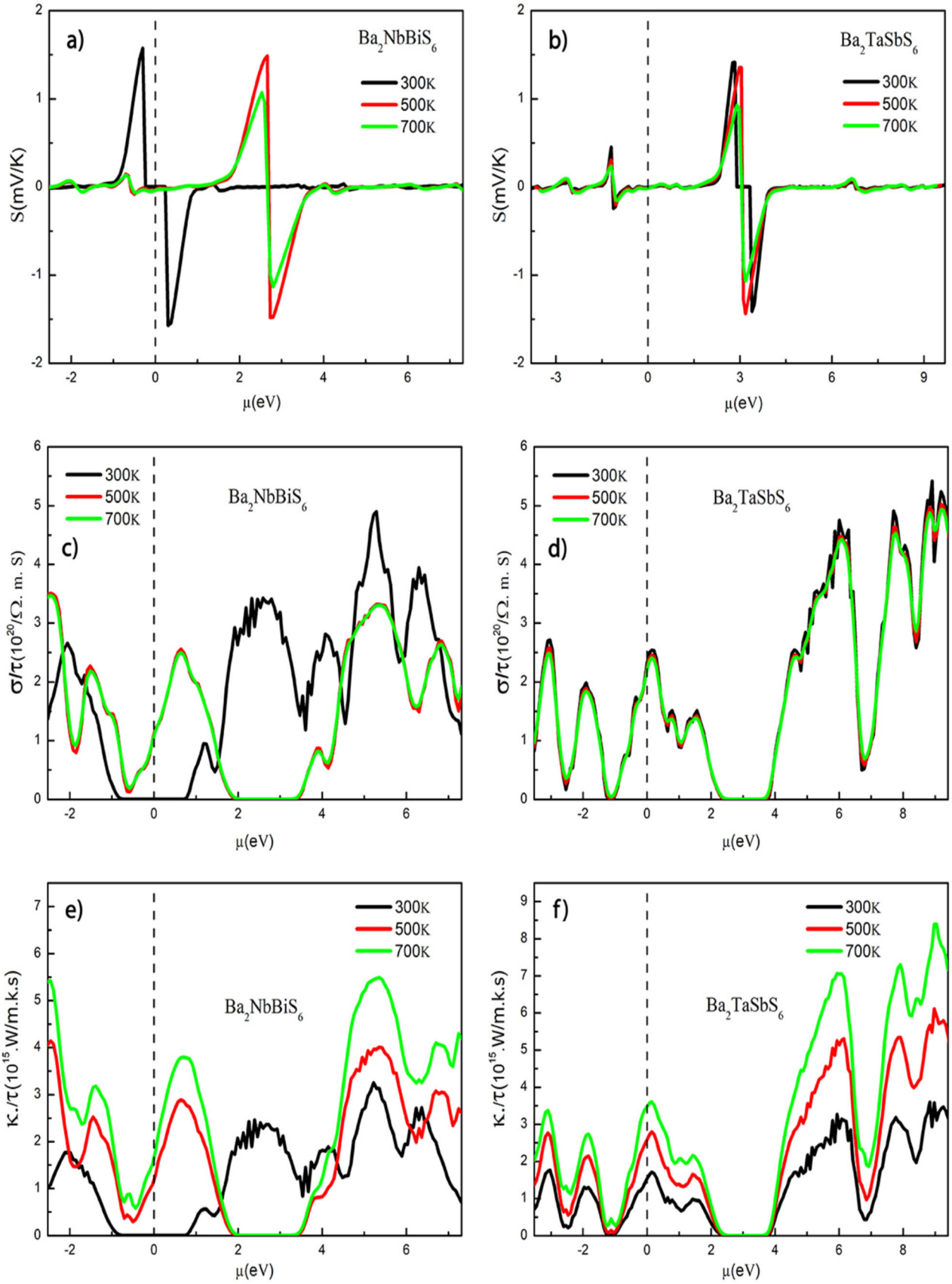
a)
Ba_2NbBiS_6
300K
500K
700K
S(mV/K)
μ(eV)
b)
Ba_2TaSbS_6
300K
500K
700K
S(mV/K)
μ(eV)
c)
Ba_2NbBiS_6
300K
500K
700K
σ/τ(10^{20}/Ω. m. S)
μ(eV)
d)
Ba_2TaSbS_6
300K
500K
700K
σ/τ(10^{20}/Ω. m. S)
μ(eV)
e)
Ba_2NbBiS_6
300K
500K
700K
κ./τ(10^{15}.W/m.k.s)
μ(eV)
f)
Ba_2TaSbS_6
300K
500K
700K
κ./τ(10^{15}.W/m.k.s)
μ(eV)

◀**Fig. 7** (**a**–**b**) Seebeck coefficient, (**c**–**d**) electrical conductivity, (**e**–**f**) electronic part of the thermal conductivity, of Ba_2NbBiS_6 and Ba_2TaSbS_6

conductivity. Although the effect of temperature on Ba_2NbBiS_6 was evident in the electrical conductivity of the system decreased with the increase in temperature, it was absent in Ba_2TaSbS_6. At 300k, the maximum value of σ/τ in p-type is 2.65×10^{20} $(\Omega ms)^{-1}$ for Ba_2NbBiS_6 and 2.71×10^{20} $(\Omega ms)^{-1}$ for Ba_2TaSbS_6, while in n-type its value is 4.89×10^{20} $(\Omega ms)^{-1}$ for Ba_2TaSbS_6 and 5.41×10^{20} $(\Omega ms)^{-1}$ for Ba_2TaSbS_6 in the μ-range of [− 2.5 to 7.3 eV]. In Fig. 8(b), the σ/τ value gradually decreases with rising temperature for both compounds, a typical behavior of semiconductors caused by increased phonon scattering, which lowers carrier mobility. The peak values are 2.32×10^{9} $(\Omega ms)^{-1}$ at 400 K for Ba_2NbBiS_6 and 2.75×10^{9} $(\Omega ms)^{-1}$ at 450 K for Ba_2TaSbS_6 before they begin to decline.

According to Fig. 7(e, f), Ba_2NbBiS_6 thermal conductivity (κ/τ) increases with varying chemical potential from the Fermi level ($\mu = 0$) at 300 K and stays constant at 500 and 700 K. At all temperatures, Ba_2TaSbS_6 shows a progressive increase in thermal conductivity with varying chemical potential. Compared to Ba_2NbBiS_6, Ba_2TaSbS_6 shows high thermal conductivity. At room temperature, the maximum value of κ/τ in p-type is 1.76×10^{15} $(\Omega ms)^{-1}$ for Ba_2NbBiS_6 and Ba_2TaSbS_6, while in n-type its value is 3.25×10^{16} $(\Omega ms)^{-1}$ for Ba_2NbBiS_6 and 3.59×10^{15} $(\Omega ms)^{-1}$ for Ba_2TaSbS_6. Figure 8(c) illustrates the κ/τ as a function of temperature increases almost linearly with temperature for both compounds, unlike σ/τ, which displays a monotonic decrease, the electronic thermal conductivity of Ba_2NbBiS_6 rising from 2.45 (W/mKs) at 300 K to 13.16 (W/mKs) at 900 K, where in the same temperature range Ba_2TaSbS_6 rising from 1.42 to 6.32 (W/mKs).

The calculated transport coefficients at 300 K, specifically the Seebeck coefficient (Fig. 7(a)), electrical conductivity (Fig. 7(c)), and electronic thermal conductivity (Fig. 7(e)), display anomalous deviations relative to the smoother temperature dependence observed at 500 and 700 K. This unexpected behavior requires careful analysis.

Physically, ambient temperature marks a critical regime in thermoelectric transport where multiple scattering processes interplay in a highly non-linear manner. Electron–phonon scattering, impurity and defect scattering, and phonon drag contribute variably to carrier relaxation times, resulting in temperature-dependent modifications of carrier mobility and effective masses [107, 108]. Such mechanisms can induce non-monotonic trends in thermoelectric coefficients. Concurrently, subtle temperature-induced changes in the electronic band structures–such as band convergence, shifts in the band edges, or the presence of flat bands near the Fermi level—can cause abrupt variations in the density of states and, consequently, in the transport integrals.

Computationally, the BoltzTraP methodology involves Fourier interpolation of density functional theory–calculated band energies combined with a constant relaxation time approximation to estimate transport coefficients [109]. While effective for many temperature ranges, this approach assumes smooth and slowly varying band dispersions near the Fermi level. However, near 300 K, rapid changes in Fermi surface topology or density of states due to band crossings or localized states can introduce numerical sensitivity or interpolation artifacts. Moreover, the neglect of temperature-dependent relaxation times in the constant relaxation time approximation limits the model's accuracy in capturing competing scattering regimes that dominate near room temperature [110, 111].

Our meticulous verification confirms that the anomaly is not due to data processing or visualization errors but rather intrinsic to the physical and numerical complexity of transport phenomena at this temperature.

In light of this, the anomaly underscores the need for future studies incorporating temperature-dependent scattering models and experimental validation near ambient conditions to better resolve the transport behavior of these materials.

The figure of merit (ZT) values are estimated using the thermal conductivity and the Seebeck coefficient [112]. Peak material figure of merit (ZT) values are frequently given, and these values may be crucial for using the specified maximum values of the merit factor (ZT) which are important indicators as they significantly influence the selection of materials for use at different temperatures. The calculated ZT and the power factor (PF) using the BoltzTraP2 code are illustrated in Fig. 8(d). It is clear that the ZT curves begin to climb at low temperatures before beginning stabilizing as the temperature rises, starting at T = 300 K with initial values of 0.22 for Ba_2NbBiS_6 and 0.08 for Ba_2TaSbS_6, and reaching a maximum of around 0.60 at 750 K and 0.36 at 900 K, respectively. Additionally, as shown in Fig. 8(e), it is worth noting that we observed a steady linear increase in the power factor coefficient (PF). At 300 K, Ba_2NbBiS_6 PF increases from 2.74×10^{10} $W^{-1} \cdot K^{-2} s^{-1}$, while Ba_2TaSbS_6 PF rises from 1.13×10^{10} $W^{-1}K^{-2}s^{-1}$ to a significantly higher value of 7.55×10^{10} $W^{-1}K^{-2}s^{-1}$ (Ba_2NbBiS_6) and 7.93×10^{10} $W^{-1}K^{-2}s^{-1}$ (Ba_2TaSbS_6) at 900 K.

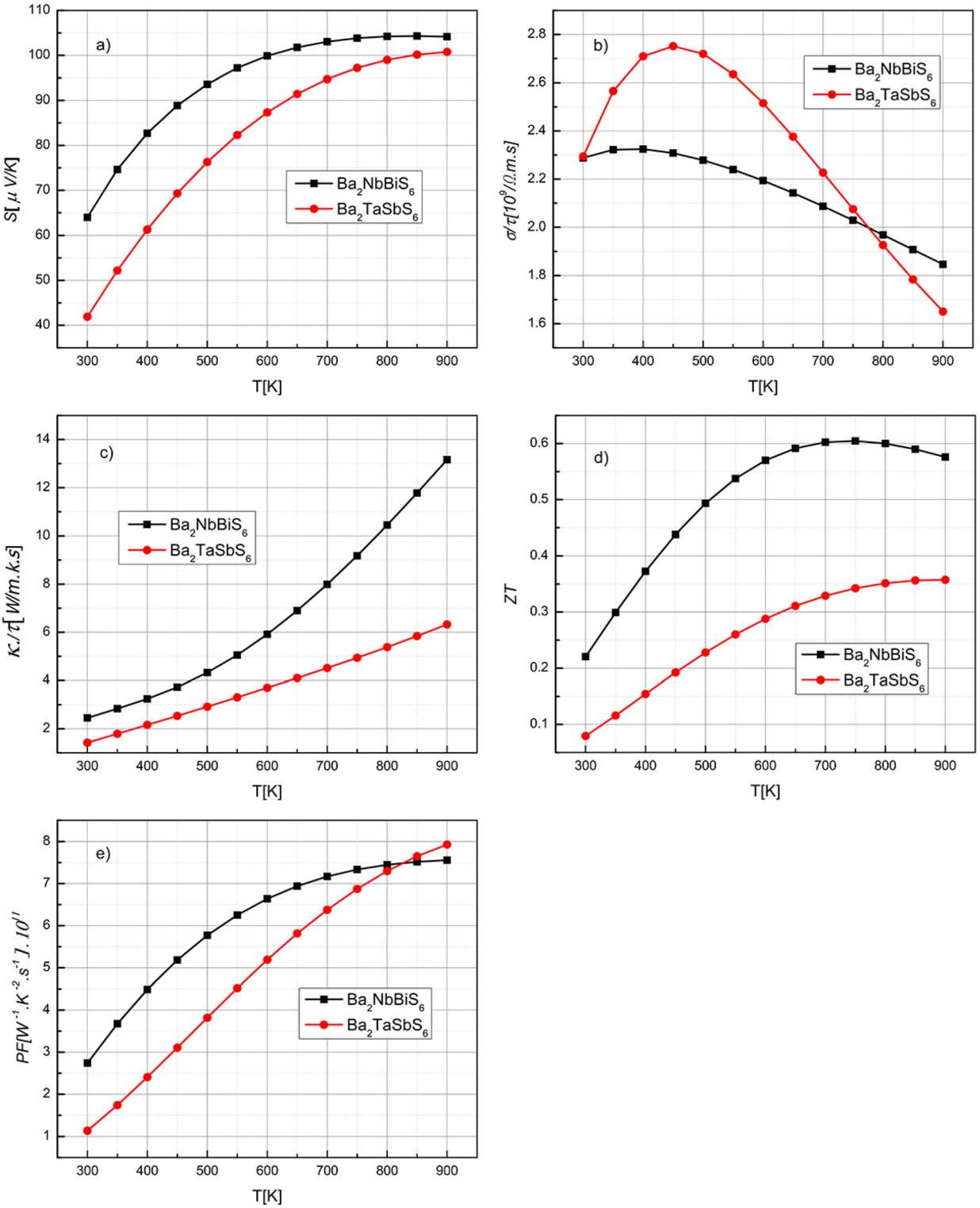

Fig. 8 (**a**) Seebeck coefficient, (**b**) electrical conductivity, (**c**) electronic part of the thermal conductivity, (**d**) ZT merit, and (**e**) power factor as a function of temperature for Ba_2NbBiS_6 and Ba_2TaSbS_6

7. Conclusion

Based on DFT calculations, this study focuses on the examination of structural, elastic, electronic, optical, and thermoelectric properties of Ba_2NbBiS_6 and Ba_2TaSbS_6 in Fm $\overline{3}$ m space group within the cubic system. The calculated lattice constants are 10.15 Å (PBE) and 10.07 Å (LDA) for Ba_2NbBiS_6 and 10.03 Å (PBE) and 9.97 Å (LDA) for Ba_2TaSbS_6. Both compounds exhibit mechanical stability, as evidenced by their compliance with Born-Huang stability criterion and their negative formation energy values. The ductile behavior of Ba_2NbBiS_6 and Ba_2TaSbS_6 is confirmed by their Pugh's ratio values of 2.23 and 2.01, respectively. The electronic characteristics validated their semiconductor nature, showing an indirect band gap (L–X) of 1.58 eV (mBJ-GGA) and 1.45 eV (mBJ-LDA) for Ba_2NbBiS_6, and an indirect band gap (L–Γ) of 1.45 eV (mBJ-GGA) and 1.28 eV (mBJ-LDA) for Ba_2TaSbS_6. The optical properties calculated using the mBJ-GGA, reveal high absorption in the visible and ultraviolet ranges with very low reflectivity. The Seebeck coefficient transition from the p-type region to the n-type region, Where Ba_2TaSbS_6 higher thermal conductivity than Ba_2NbBiS_6. Overall, the thermoelectric performance demonstrates that Ba_2NbBiS_6 is the most efficient candidate achieving a higher figure of merit (ZT = 0.60). The relatively large band gap and higher ZT value confirm that Ba_2NbBiS_6 is a promising candidate for thermoelectric and optoelectronic applications, including the solar cell devices.

Acknowledgements We sincerely thank all the collaborators who contributed to this project. Our gratitude also goes to the General Directorate for Scientific Research and Technological Development in Algeria. This study was conducted as part of the PRFU project number A10N01UN280120220006.

Author's contributions Hamza Bennacer proposed the research idea and followed the whole process, checking and reviewing it. Zakarya Bouguerra and Inas Bouzateur wrote the main body of the manuscript and conducted analysis. Abdelkader Boukortt, Mohammed Assam Ouali, Moufdi Hadjab, and Mohamed Issam Ziane revised the paper and providing additional comments.

Data availability This article includes all data produced or analyzed during this study. Extra data will be made available on request.

Declarations

Conflict of interest The authors confirm that they have no financial or competing interests related to this research.

References

[1] S M H Qaid et al. Materials Science and Engineering: B 301 (2024).
[2] H Murtaza et al. Physica B Condens Matter 677 (2024).
[3] M Tariq, M A Ali, A Laref, and G Murtaza Solid State Commun 314 (2020).
[4] H Murtaza et al. Solar Energy 273 (2024).
[5] I Bouzateur, M A Ouali, H Bennacer, M Ladjal, M A A Rahman and A Boukortt Mater Today Commun **37** 107021 (2023).
[6] H J Snaith Journal of Physical Chemistry Letters **4** 3623 (2013).
[7] T M Brenner, D A Egger, L Kronik, G Hodes and D Cahen Nat Rev Mater 1 (2016).
[8] M A Green et al. Jiang Progress in Photovoltaics: Research and Applications (2024).
[9] K Li et al. Adv Energy Mater **15** 2404335 (2025).
[10] H Murtaza, Q Ain, T Akhter and J Munir J Power Sources **641** 236788 (2025).
[11] I Mursaleen, J Munir, Q Ain, I Albrahee, S M H Qaid, and A S Aldwayyan J Mater Res 1 (2025).
[12] Q A Akkerman, Kovalenko and L Manna Nat Mater **17** 394 (2018).
[13] C Li et al. Light Sci Appl 9 (2020).
[14] M A Green, A Ho-Baillie and H J Snaith Nat Photonics **8** 506 (2014).
[15] Q Chen et al. *Nature* **561** 88 (2018).
[16] M A Green Silicon solar cells: evolution, Semiconductor Science and Technology, **8** 1 (1993).
[17] J J Yoo et al. *M G Bawendi, and J Seo Nature* **590** 587 (2021).
[18] V Chauhan et al. Inorg Chem Commun 157 (2023).
[19] A Chilvery, S Palwai, P Guggilla, K Wren and D Edinburgh Perovskite Materials, Devices and Integration (2020).
[20] W-J Yin, J-H Yang, J Kang, Y Yan and S-H Wei Journal of Materials Chemistry A 3 8926 (2015).
[21] A H Slavney, R W Smaha, I C Smith, D Umeyama and H I Karunadasa Inorg Chem **56** 46 (2017).
[22] M Husain et al. J Lu Inorg Chem Commun 164 (2024).
[23] Q Dai et al. Mater Sci Semicond Process **185** 108930 (2025).
[24] Q Dai, Q Q Liang and T Y Tang, S Q Wu and Y L Tang Inorg Chem Commun **166** 112591 (2024).
[25] S Khawar et al. Journal of Materials Research and Technology **21** 4790 (2022).
[26] S Khawar et al. Phys Scr **98** 115919 (2023).
[27] D O Obada et al. Crystals (Basel) 14 (2024).
[28] B Inas, B Hamza, O M Assam, L Mohamed, Z M Issam and H Moufdi Proceedings of the 2022 International Conference of Advanced Technology in Electronic and Electrical Engineering, ICATEEE 2022 (2022).
[29] H U Rehman et al. Sens Actuators A Phys **393** 116866 (2025).
[30] H U Rehman, N Muhammad, G Murtaza, H H Raza, M Irfan and M A Rehman Opt Quantum Electron **56** 1 (2024).
[31] H Lin et al. Adv Funct Mater 34 (2024).
[32] J Munir et al. Materials Science and Engineering: B 298 (2023).
[33] H M Ghaithan, S M H Qaid, Z A Alahmed, H S Bawazir and A S Aldwayyan Materials 16 (2023).
[34] H U Rehman et al. Mater Today Commun **40** 109806 (2024).
[35] Y Y Sun, P Zhang and S Zhang Nano Lett **15** 581 (2015).
[36] W Meng, B Saparov, F Hong, D B Mitzi and Y Yan Chemistry of Materials **28** 821 (2016).
[37] S Niu et al. Advanced Materials 29 (2017).
[38] M G Ju, J Dai, L Ma and X C Zeng Adv Energy Mater 7 (2017).
[39] Z Bouguerra, H Bennacer, A Boukortt, A H Denawi and S Meskine Computational Condensed Matter 41 (2024).
[40] H Murtaza, J Munir, Q Ain, A S Aldwayyan, A A Ali Ahmed and S M H Qaid Solar Energy 290 (2025).
[41] H Baaziz, T Ghellab and Z Charifi Int J Mod Phys B (2024).

[42] H U Rehman, M U Abdullah and A Usman Chem Phys **598** 112841 (2025).
[43] M Noman, R Neffati, S Khan, M W Ashraf and G Murtaza Physica B Condens Matter **656** 414779 (2023).
[44] S Niaz, M A Khan, H Ullah and R Neffati Journal of Physics and Chemistry of Solids **174** 111115 (2023).
[45] Q Sun, H Chen and W J Yin Chemistry of Materials 31 244 (2019).
[46] M L. Agiorgousis, Y Y Sun, D H Choe, D West and S Zhang Adv Theory Simul 2 (2019).
[47] E T McClure, M R Ball, W Windl and P M Woodward Chemistry of Materials 28 1348 (2016).
[48] A H Slavney, T Hu, A M Lindenberg and H I Karunadasa J Am Chem Soc 138 2138 (2016).
[49] G Volonakis, M R Filip, A A Haghighirad, N Sakai, H J Snaith and F Giustino Journal of Physical Chemistry Letters **7** 1254 (2016).
[50] W Deng et al. Appl Phys Lett 111 (2017).
[51] G Volonakis et al. Journal of Physical Chemistry Letters **8** 772 (2017).
[52] M A Ali, A Alodhayab, S Mohammad and M Faizan Energy Technology 11 (2024).
[53] P Blaha, K Schwarz, F Tran, R Laskowski, G K H Madsen and L D Marks Journal of Chemical Physics 152 (2020).
[54] L Nordström, G K H Madsen, P Blaha, K Schwarz and E Sjöstedt Phys Rev B Condens Matter Mater Phys 64 (2001).
[55] P Hohenbergt, W Kohn PHYSICAL REVIEW **136** 864 (1964).
[56] W Kohn and LJ Sham Physical Review A **140** 1133 (1965).
[57] J P Perdew et al. Phys Rev Lett **100** 136406 (2008).
[58] J P Perdew and Y Wang Phys Rev B **45** 13244 (1992).
[59] D Danovich, S Shaik and H Chen Comprehensive Inorganic Chemistry II (Second Edition): From Elements to Applications **9** 1 (2013).
[60] A W Götz, T Wölfle and R C Walker Annu Rep Comput Chem **6** 21 (2010).
[61] F Tran and P Blaha Phys Rev Lett 102 (2009).
[62] G K H Madsen, J Carrete and M J Verstraete Comput Phys Commun **231** 140 (2018).
[63] A D Becke and M R Roussel Phys Rev A (Coll Park) **39** 3761 (1989).
[64] Y Mamouni, H Bennacer, A Boukortt, A H Denawi and N El Houda Habibes Mater Today Commun **41** 110508 (2024).
[65] M J I Khan et al. Commun Theor Phys 73 (2021).
[66] Q A Akkerman, D Meggiolaro, F De Angelis and L Manna ACS Energy Lett **2** 2183 (2017).
[67] A Halder, A Ghosh and T S Dasgupta Phys Rev Mater 3 (2019).
[68] C J Bartel et al. Sci Adv 5 (2019).
[69] G G C Peterson and J Brgoch JPhys Energy 3 (2021).
[70] C Firat Future Sustainability **3** 26 (2025).
[71] D Y Hu et al. Solid State Chem 310 (2022).
[72] F Mouhat and F-X Coudert *Physical Review B* **90** 224104 (2014).
[73] C Zhao, X Wang and J Alloys *Compd* **704** 484 (2017).
[74] S A Dar and B Want Micro and Nanostructures 170 (2022).
[75] S Guo et al. Mater Sci Semicond Process 177 (2024).
[76] K Bouferrache et al. Results Phys 56 (2024).
[77] S Mender, M Labidi, S Labidi, R Masrour and M Ellouze Computational Condensed Matter 40 (2024).
[78] X Du, D He, H Mei, Y Zhong and N Cheng Physics Letters, Section A: General, Atomic and Solid State Physics 384 (2020).
[79] S Yalameha, Z Nourbakhsh and D Vashaee Comput Phys Commun 271 (2022).
[80] T Ghellab, Z Charifi and H Latelli Physica B Condens Matter **653** 414678 (2023).
[81] J Haines, J M Léger and G Bocquillon Annual Review of Materials Research 31 1 (2001).
[82] Z Ye, F Jia, S Xu, H Su and W Ren J Mater Res **39** 903 (2024).
[83] X Hao, Y Xu, Z Wu, X Liu and J Meng J Alloys Compd **453** 413 (2008).
[84] S A Khan, H U Khan, S Mehmood and Z Ali Mater Sci Semicond Process 122 (2021).
[85] R Zada, Z Ali and S Mehmood Mater Sci Semicond Process 147 (2022).
[86] H M Tahir Farid et al. Journal of Materials Research and Technology 13 1485 (2021).
[87] S Naz, Z Ali, S Mehmood, I Khan and I Ahmad Mater Sci Semicond Process 132 (2021).
[88] H A Alburaih et al. Appl Phys A Mater Sci Process 128 (2022).
[89] M Akhtar et al. Physica B Condens Matter **700** 416937 (2025).
[90] H Murtaza et al. Journal of Physics and Chemistry of Solids 198 (2025).
[91] S Wang, Y Xu, X Guo and C Nan Physica B Condens Matter **550** 347 (2018).
[92] A Ayyaz et al. Ceram Int **50** 15261 (2024).
[93] M A Ali et al. Journal of Physics and Chemistry of Solids 159 (2021).
[94] B Ul Haq, S AlFaify, R Ahmed, A Laref, Q Mahmood and E Algrafy Appl Surf Sci 525 (2020).
[95] Q Mahmood, T Ghrib, A Rached, A Laref and M A Kamran Mater Sci Semicond Process 112 (2020).
[96] U G Jong, C J Yu and Y H Kye RSC Adv **10** 201 (2019).
[97] M Gajdoš, K Hummer, G Kresse, J Furthmüller and F Bechstedt Phys Rev B Condens Matter Mater Phys 73 (2006).
[98] Y Shen and Z Zhou J Appl Phys 103 (2008).
[99] M Dadsetani and A Pourghazi Phys Rev B Condens Matter Mater Phys 73 (2006).
[100] M Elamin Ketfi, H Bennacer, S S Essaoud, M Issam Ziane and A Boukortt Mater Chem Phys 277 (2022).
[101] M I Ziane et al. Optik (Stuttg) **243** 167490 (2021).
[102] Q Mahmood et al. Phys Scr 97 (2022).
[103] M J I Khan, J Liu, Z Kanwal, M I Khan, M N Usmani and A U R Khalid Mater Res Express 7 (2020).
[104] M A Ali, T Alshahrani and G Murtaza Mater Sci Semicond Process 127 (2021).
[105] H Albalawi et al. Mater Today Commun 32 (2022).
[106] N A Noor, M Rashid, G M Mustafa, M I Khan, A Mahmood and S M Ramay Chem Phys Lett 753 (2020).
[107] G D Mahan Solid State Physics - Advances in Research and Applications **51** 81 (1998).
[108] J M Ziman Electrons and Phonons (2001).
[109] G K H Madsen and D J Singh Comput Phys Commun **175** 67 (2006).
[110] Y Pei, X Shi, A Lalonde, L Chen and G J Snyder Nature **473** 66 (2011).
[111] G J Snyder and E S Toberer *Nat Mater* **7** 105 (2008).
[112] A Jabar, S Benyoussef and L Bahmad Optik (Stuttg) 311 (2024).
[113] H Bendjilali, A Chahed, M N Bousahla and Y A Khachai Annals of West University of Timisoara - Physics **64** 37 (2022).

[114] N Rajamanickam, S Rajashabala and K Ramachandran AIP Conference Proceedings 1667 080034 (2015)